

# Molecular dynamics approach for predicting release temperatures of noble gases in pre-solar nanodiamonds

Alireza Aghajamali<sup>1,\*</sup> and Nigel A. Marks<sup>1</sup>

<sup>1</sup>*Department of Physics and Astronomy, Curtin University, Perth, Western Australia 6102, Australia*

(Dated: October 27, 2021)

Pre-solar meteoritic nanodiamond grains carry an array of isotropically anomalous noble gas isotopes and provide information on the history of nucleosynthesis, galactic mixing and the formation of the solar system. In this paper, we develop a molecular dynamics approach to predict thermal release distribution of implanted noble gases (He and Xe) in nanodiamonds. Our simulations show that low-energy ion-implantation is a viable way for the incorporation of noble gases into nanodiamonds. Accordingly, we provide atomistic details of the unimodal temperature release distribution for helium and a bimodal behavior for xenon. Intriguingly, our model shows that the thermal release process of noble gases is highly sensitive to the impact and annealing parameters as well as to crystallographic orientation. In addition, the model elegantly explains the unimodal and bimodal behaviour via the interstitial and substitutional types of defects formed. In particular, our approach explains the origin of the famous Xe-P3 and Xe-HL peaks, and shows that P3 component in meteoritic literature releases not only at the low-temperature but also at the high-temperature along with HL component. This means that an isotopically anomalous HL component must be the sum of high temperature part of P3 component and a pure-HL component.

## I. INTRODUCTION

Nanodiamonds are common grains in primitive chondritic meteorites [1], with abundances as high as 1500 ppm [2–5]. Trace quantities of xenon and other noble gases found within the nanodiamonds (NDs) have isotopic distributions significantly different to terrestrial abundances, providing strong evidence that the NDs, and hence the meteorites, are pre-solar. To quantify the noble gas composition, the NDs are chemically separated from the host meteorite, pyrolyzed to release the gases and then analyzed with a mass spectrometer. Typically, one in every million NDs will contain a xenon atom, and one in ten will contain a helium [6]. Stepped pyrolysis reveals that light elements (helium and neon) have a temperature-release distribution comprising a single broad peak, while for heavy elements (argon, krypton and xenon) the thermal-release distribution is bimodal.

The bimodal character of the thermal-release during stepped pyrolysis has commonly been attributed to the presence of different components of xenon. The low-temperature peak around 500°C has an isotopic distribution close to terrestrial abundances and is referred to as P3, while the high-temperature peak around 1420°C is isotopically anomalous [3, 7] and known as HL due to an excess of Heavy and Light isotopes. The other heavy noble gases (i.e. argon and krypton) also exhibit bimodal behaviour, with the same release temperatures and isotopic anomalies. These isotopic anomalies have been extensively studied, since pre-solar material provides information on the history of nucleosynthesis and galactic mixing. For xenon, an excess of heavy and light isotopes is consistent with *r*- and *p*-processes in super-

nova nucleosynthesis [8–10].

Understanding the origin and meaning of the P3 and HL components has proved challenging due to difficulties in identifying the specific processes responsible for (a) incorporation of the noble gas, and (b) gas release during pyrolysis. While one possibility is that the noble gases were trapped during growth of the NDs, the most popular explanation for incorporation is an implantation-type process where noble gases are driven into pre-existing NDs [2, 11–13]. The strongest support for the latter hypothesis comes from Koscheev *et al.* [14] who implanted a low energy ( $\sim 700$  eV) noble gas ions into synthetic NDs. Pyrolysis measurements observed a single broad temperature distribution for He and Ne, and a bimodal distribution for Ar, Kr and Xe, corresponding closely to those found for meteoritic NDs [3, 7]. Even though the implantations involved gases with terrestrial abundances, a bimodal temperature-release distribution was found. Similar studies by Verchovsky *et al.* [15] also found a bimodal distribution. This suggests that the P3 and HL components were probably implanted via different events at different stages in the history of the ND grains.

In this work, we use the Molecular Dynamics (MD) approach and apply it to the question of the single and bimodal temperature-release of noble gases. To the best of our knowledge, atomistic simulation methods have not previously been applied to this problem. We simulate the implantation and pyrolysis processes for helium and xenon, and find excellent agreement with experimental data collected from meteorites. We reproduce the single release peak for helium and bimodal release for xenon. The simulations explain how the mass, implantation depth and crystallographic location of the noble gases gives rise to the experimental observations, and for the first time provide an atomistic explanation of the release mechanism.

Our paper is structured as follows. In the Methodology

---

\* alireza.ghajamali@curtin.edu.au

we introduce our MD approach, which includes an Arrhenius framework to map the simulation temperatures onto their experimental equivalent. Our first of results are qualitative, using visualization and movies of the implantation and thermal-release processes to highlight the differences between helium and xenon. The second set of results involves robust statistical analysis of a large number of simulations spanning many implantation energies, implantation directions and annealing temperatures. The final section uses the Arrhenius approach to make direct comparison between meteoritic data and the simulations.

## II. METHODOLOGY

### A. Simulation methods

The Molecular Dynamics simulations are performed using the Environment Dependent Interaction Potential (EDIP) [16] for carbon-carbon interactions in combination with the standard Ziegler-Biersack-Littmark (ZBL) potential [17] to describe close approaches. EDIP has proved itself to be highly transferable [18, 19] and has previously been successful in simulations of many different forms of carbon such as diamond [20–23], carbon onions [24], amorphous carbon [25], glassy carbon [26, 27], nanotubes [28], peapods [29] and carbide-derived carbons [30, 31]. To describe helium-carbon and xenon-carbon interactions, we use a Lennard-Jones (LJ) potential coupled with the ZBL potential, with interpolation between the two interactions controlled using Fermi-type switching functions as described in Buchan *et al.* [22] and Christie *et al.* [32]. This combination of the LJ and ZBL potentials is identical to our recent article [33] where we studied the modification of NDs by xenon implantation. Full details are provided in the Supplementary Material.

We perform our simulations using an in-house MD package. All calculations are carried out in an NVE ensemble (meaning number of particles ( $N$ ), volume ( $V$ ) and energy ( $E$ ) are conserved quantities), using Verlet integration and a variable timestep [34]. Periodic boundary conditions are not employed. All simulations use a 4999-atom ND with a diameter of 3.9 nm; this size is similar to synthetic and meteoritic NDs [3, 7, 14]. As shown in Fig. 1, the ND has a truncated octahedral form which is the stable geometry for dehydrogenated NDs [35]. The  $\{100\}$  faces of the ND are reconstructed in a  $2\times 1$  manner to eliminate dangling bonds. The coordinates of the ND were generated using a methodology described in our recent article studying xenon implantation [33]. The key idea is to cut the ND out of an infinite crystal using clipping planes in the  $\langle 100 \rangle$  and  $\langle 111 \rangle$  directions. Using the notation of Fogg *et al.* [33], the ND used in this work was generated with  $d_{100}=20$  Å and  $d_{111}=17$  Å. Prior to implantation, the ND is equilibrated at 300 K.

Implantation simulations are 1 ps in length, sufficient to model the ballistic phase of ion implantation into the

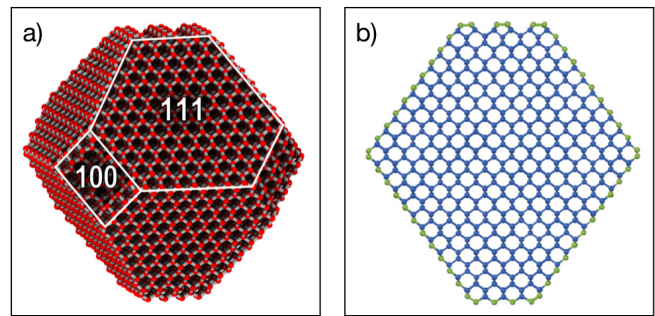


FIG. 1. Two views of the 3.9 nm diameter ND used in this work. (a) Perspective view showing the truncated octahedral geometry. Carbon atoms are shown in red and the white lines highlight the  $\{100\}$  and  $\{111\}$  faces. (b) Cross-sectional view (1 nm slice) using color coding to indicate the hybridization:  $sp^2$  and  $sp^3$  atoms are shown as green and blue circles, respectively. Note that the  $\{100\}$  faces are reconstructed in a  $2\times 1$  manner to eliminate dangling bonds.

ND. To generate a wide variety of implantation conditions, the initial position and direction of the implanted species (either helium or xenon) was systematically varied. Following our previous studies [22, 32, 33, 36], the initial position is taken from a 25-point solution to the Thomson problem [37] which distributes coordinates uniformly on a sphere. Some implantations are performed directly towards the centre of the ND, while others are directed slightly (up to 10 Å) away from the centre-of-mass. After the system equilibrates, the implantation depth is computed relative to the nearest crystallographic face,  $\{100\}$  or  $\{111\}$ . For the helium implantations the mass was 4 amu, while the xenon implantations use a mass of 133 amu, the same as in [33, 36] and slightly higher than the average isotopic value of 131.3 amu. Additional xenon simulations use masses of 124 and 136 amu, corresponding to the lightest and heaviest stable isotopes.

Annealing simulations extending up to 1 ns are performed to study the thermal release process. Coordination analysis is performed by counting the number of nearest neighbours within a cutoff of 1.85 Å. For the purposes of analysis and visualization, atoms are considered to be  $sp$ ,  $sp^2$  and  $sp^3$  hybridized if they have two, three and four neighbours, respectively. Visualization is performed using the OVITO package [38].

### B. Mapping to experimental temperatures

Generally speaking, the timescale of MD simulations are on the order of nanoseconds, around 13 orders shorter than the experimental annealing time. This enormous difference complicates comparison between simulations and experiments, as thermally activated events will be suppressed in the simulations due to vastly shorter time. Many different solutions to the MD timescale problem have been proposed [39–41], but here we employ a sim-

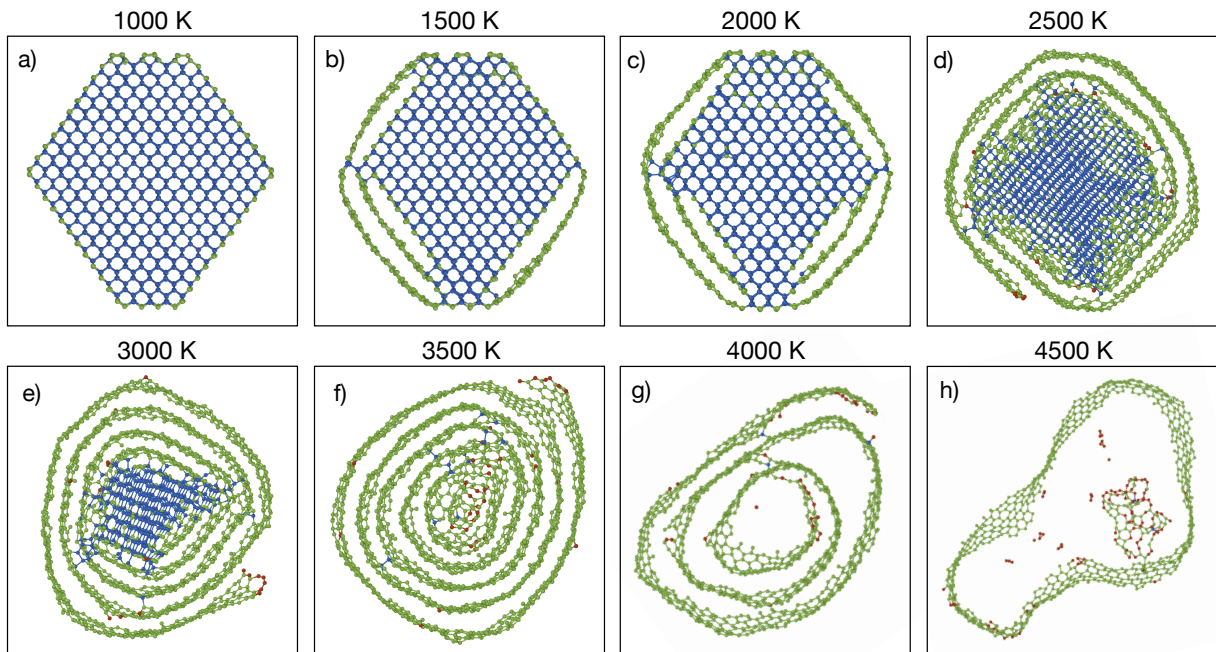


FIG. 2. Cross-sectional snapshots (1 nm slices) of pristine ND after annealing for 1 ns at various temperatures. Panel (f) shows that at 3500 K the experimentally observed result, namely a carbon onion, is obtained. Red, green and blue circles denote  $sp$ ,  $sp^2$  and  $sp^3$  hybridization, respectively. Full discussion of the onionization process is provided in the Supplementary Material.

ple temperature-acceleration approach that we have used successfully on other carbon systems [30]. The first step is to assume Arrhenius behavior and a single activation energy, which corresponds to the relation

$$f = A \exp(-E_a/k_B T) \quad (1)$$

where  $f$  is the frequency of events,  $A$  is the attempt frequency,  $T$  is the temperature,  $k_B$  is Boltzmann's constant and  $E_a$  is the activation energy. The correspondence between the experimental and simulation temperature is determined by equating the time-frequency product (i.e.  $f_{\text{expt}} \times t_{\text{expt}} = f_{\text{sim}} \times t_{\text{sim}}$ ) to ensure that for the same activation energy the same number of events occur in both simulation and experiment. This yields the following expression

$$T_{\text{sim}} = -\frac{E_a}{k_B} \times \left[ \log\left(\frac{t_{\text{expt}}}{t_{\text{sim}}}\right) - \frac{E_a}{k_B T_{\text{expt}}} \right]^{-1} \quad (2)$$

This equation links the experimental temperature and time ( $T_{\text{expt}}$  and  $t_{\text{expt}}$ ) with those of the simulation ( $T_{\text{sim}}$  and  $t_{\text{sim}}$ ) with the only parameter being the activation energy. To determine  $E_a$ , we make use of experimental data on graphitization of NDs, where it is known that  $\sim 1500^\circ\text{C}$  is required to convert NDs into a carbon onion [42–46]. To identify the corresponding temperature on the MD timescale we performed a set of 1 ns simulations at different annealing temperatures and found that onionization of the ND occurs at around 3500 K (see Fig. 2). Using these two temperatures and suitable times

( $t_{\text{sim}}=10^{-9}$  s and  $t_{\text{expt}}=3600$  s [42–46]), we obtain via Eq. 2 a value of  $E_a=9$  eV. Having determined the activation energy, we can employ Eq. 2 to map any simulation temperature to its experimental equivalent using the relation shown in Fig. 3. For example, the pink lines in the figure show that a simulation temperature of 4500 K is equivalent to an experimental temperature of  $\sim 1730^\circ\text{C}$ , and a simulation at 2000 K is equivalent to an experiment at  $\sim 1000^\circ\text{C}$ . The latter also serves as a convenient dividing line between the P3 and HL peaks for xenon [3, 7]. To provide a sense of scale, Fig. 3 also shows calibration curves for two other activation energies. Note that due to the logarithm term in Eq. 2 the value of  $E_a$  has minimal sensitivity to the choice of  $t_{\text{expt}}$ . This point is discussed in detail in de Tomas *et al.* [30]. Finally, we note that throughout this manuscript we adopt the convention that experimental temperatures are given in Celsius and simulation temperatures are in Kelvin. This helps conceptually separate the two quantities which otherwise might be confused with one another.

### III. RESULTS AND DISCUSSION

#### A. Individual implantation and thermal release events

Representative examples of the implantation and thermal release processes for helium and xenon are shown in Fig. 4. Panels (a) and (c) show that the implantation

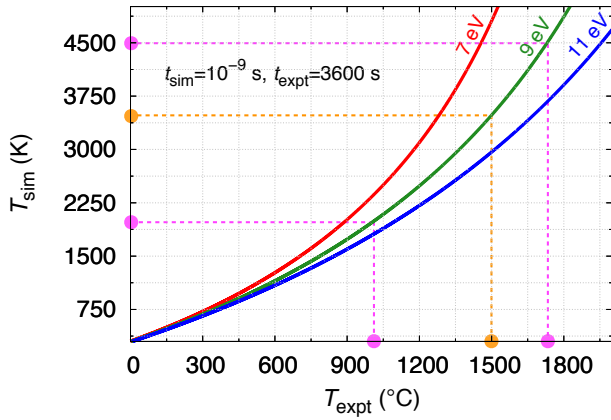


FIG. 3. Calibration curve between simulation and experimental temperatures via the Arrhenius approach. The orange dashed line indicates data for the onionization of a ND used to determine the value of  $E_a=9$  eV. The pink lines indicate two examples of the mapping process as described in the text.

processes for helium and xenon differ substantially, with the higher mass and size of the xenon having a large effect. For helium, only a relatively modest of energy ( $\sim 100$  eV) is needed to implant the atom into the centre of the ND, and the helium undergoes multiple deviations along the implantation trajectory (pink line) since the

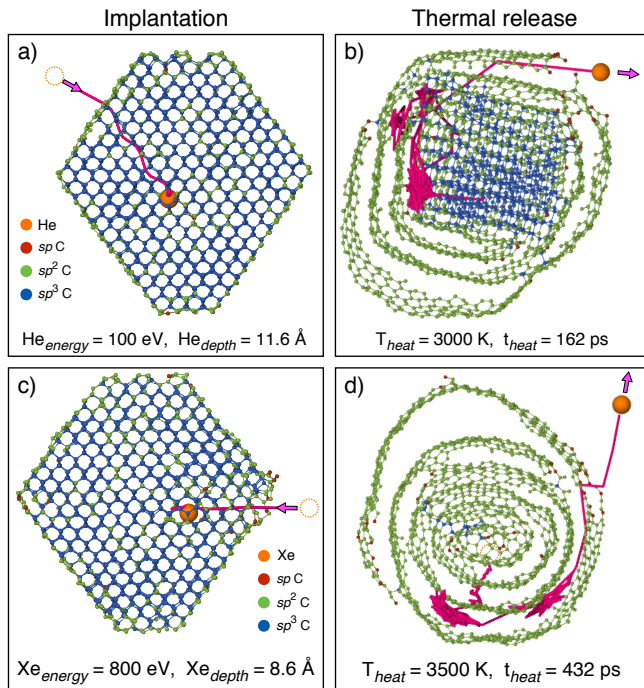


FIG. 4. Typical implantation (left panels) and thermal release (right panels) processes involving helium [panels (a) and (b)] and xenon [panels (c) and (d)]. The pink lines indicate the helium and xenon trajectories, and the helium and xenon are shown as an orange circles. The color codings and cross-sectional slice details are the same as Fig. 2.

carbon atoms are three times heavier. In contrast, the implanting xenon simply slows down, and it is the carbon atoms which move. Around  $\sim 800$  eV of kinetic energy is needed to implant into the central region, similar to the value of circa 700 eV used by Koscheev *et al.* [14] in their experiments.

Once the implanted ND system has equilibrated, the entire cluster is heated to to find the temperature at which the noble gas atom escapes. Examples of this process are shown in panels (b) and (d). For both species, thermal release occurs at relatively high simulation temperatures; 3000 K for helium and 3500 K for xenon. As seen in Fig. 2, these temperatures are sufficient to transform portions of the ND into a onion-like structure. Due to its small size, the helium is able to escape before the ND has completely onionized. The complexity of the process can be appreciated in Supplementary Movie S1 which shows how the helium travels along multiple  $\langle 110 \rangle$  channels, and traverses a substantial fraction of the nanodiamond before escaping. In the case of xenon, the ND is fully transformed into a carbon onion and the release process is more difficult as the xenon must pass through the graphitic shells. The pink trajectory in panel (d) shows that the release process involves two local minima in which the xenon jiggles back-and-forth many times before escaping. An animation sequence of this process is provided in Supplementary Movie S2.

To determine the temperature at which helium and xenon are released we perform 1 ns annealing simulations at many different temperatures and monitor the distance between the noble gas species and the center of the mass of the system. An example of our methodology is provided in Figure 5 which shows this quantity ( $r_{c.m.}$ ) for xenon as a function of time for three different annealing temperatures, using the implanted ND in Fig. 4(c) as the starting structure. At 3000 K (blue line) the xenon remains the same distance from the center of

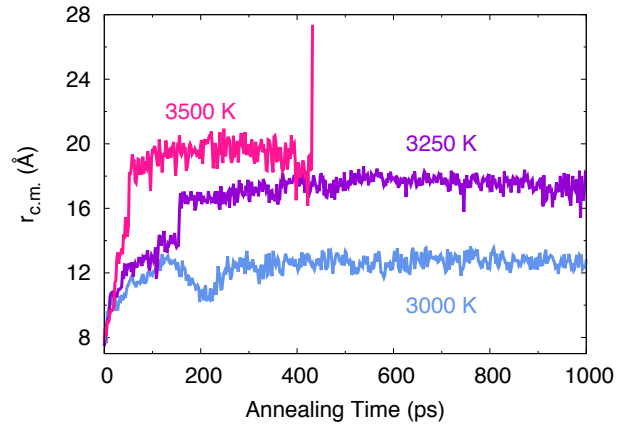


FIG. 5. Distance between xenon and the center of mass of the ND as a function of annealing time for three different annealing temperatures. The structure in Fig. 4(c) is the starting point for all three simulations.

mass. This occurs because the xenon becomes trapped at the interface between the ND core and onionized outer layers (see Fig. 2(e)). At 3250 K (violet line) the xenon moves towards the surface of the ND during the first  $\sim 170$  ps of annealing, but afterwards it is trapped between the graphitic shells. Note that at around 30 and 160 ps, there are two significant surges in  $r_{c.m.}$  where the xenon atom passes through the graphitic shells. At 3500 K (pink line), the xenon is initially trapped between graphitic shells, but after moving between them, finally exits through a gap in the outer shell at 432 ps, producing a sharp jump in  $r_{c.m.}$ .

### B. Statistical analysis

To collect a statistically significant data set a large number of implantation and thermal release simulations need to be performed. The first step is to perform simulations that implant helium and xenon into a wide variety of configurations within the ND. For each species a total of 1875 implantations were performed; 25 different energies, each with 75 different initial conditions (i.e. directions and/or impact parameters). A summary of the resultant implantation depth and incorporation probability is shown in Fig. 6. Panels (a) and (b) show the implantation depth of helium and xenon as a function of implantation energy, where each dot indicates an implantation event whereby the noble gas species remains with the ND. Impacts where the helium or xenon leave the ND are not shown. The fewest dots occur for high helium implantation energies (where helium passes through the ND) and low xenon implantation energies (where xenon is reflected). The distribution of depths differs considerably between the two species. For helium, the implantation depth spans the maximum possible range, extending from the surface to the centre of the ND, and the implantation depth is uncorrelated with energy. In contrast, low energies result in only shallow implantation of xenon, while nearly 600 eV is required to span the full range of depths. High xenon implantation energies still produce a large number of shallow implantation depths, which is perhaps due to the small size of the ND.

Figure 6(c) quantifies the incorporation probability of helium and xenon as a function of implantation energy. The probabilities for the two species are strikingly different, and are driven by the mass difference relative to carbon. This data shows that low energies are optimal for helium implantation, while efficient xenon implantation requires many hundreds of eV. Noting that helium is the most abundant noble gas in meteoritic NDs [6], this data imposes constraints on the astrophysical conditions for helium incorporation via implantation. In the case of xenon, the simulation data confirms the experimental observations of Koscheev *et al.* [14] that circa 700 eV is a suitable energy for implanting xenon into NDs.

The second step in performing the statistical analysis uses the coordinates associated with each dot in Fig. 6

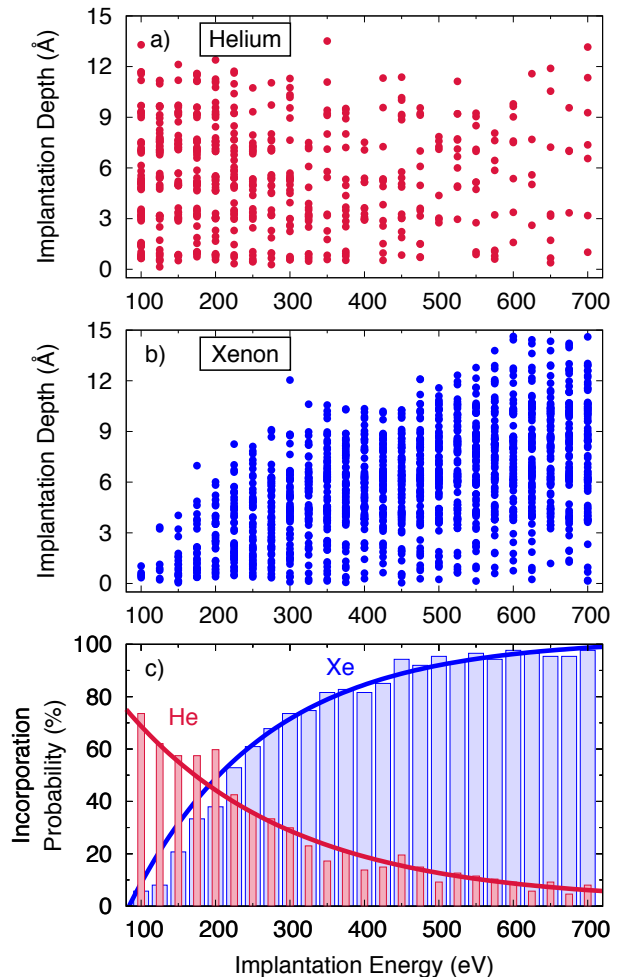


FIG. 6. Implantation depth of (a)  $^4\text{He}$  and (b)  $^{133}\text{Xe}$  as a function of implantation energy. Panel (c) shows the incorporation probability of implanted helium (red) and xenon (blue) as a function of implantation energy. The solid lines in (c) are exponential fits to guide the eye, and have decay constants of 0.22 and 0.16 eV for helium and xenon, respectively.

as the starting structure of thousands of thermal release simulations. All simulations run for 1 ns, except for when  $r_{c.m.}$  indicate that release has occurred; in such cases the simulation is terminated. If thermal release does not occur, the simulation is rerun at a higher temperature. Typically, the temperature increment between successive simulations is 100–250 K. The raw simulation data showing the relationship between the release temperature of the noble gas and the implantation depth is shown in Fig. 7. The dots and error bars indicate the precision, meaning that if a noble gas atom releases at a temperature  $T_2$  but not at a lower temperature  $T_1$ , then the dot denotes  $(T_1 + T_2)/2$  and the error bar indicates the range  $[T_1 : T_2]$ . Panel (b) shows that the xenon release temperatures cluster into two groups and correlate with the depth of the implanted atom. The average temperature for these two clusters are indicated by the green lines, with a dividing line of 2000 K used to separate the

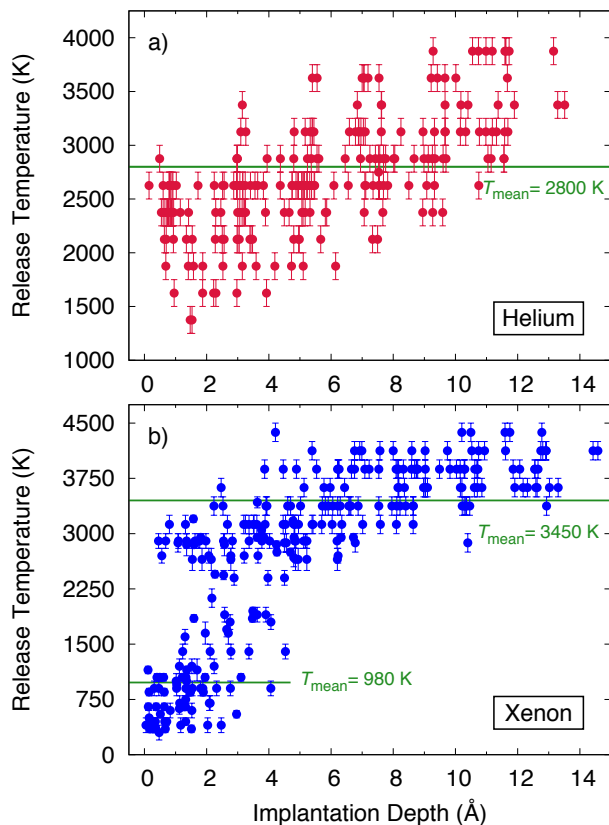


FIG. 7. Thermal release data of (a)  $^4\text{He}$  and (b)  $^{133}\text{Xe}$  as a function of implantation depth. Mean release temperatures ( $T_{\text{mean}}$ ) are shown by horizontal green lines and error bars indicate the degree of uncertainty; the precise meanings are explained in the text.

groups. Varying this number by several hundred Kelvin makes little difference to the averages. For helium, no clustering occurs, and the release temperature gradually increases with implantation depth. In this case the green line indicates the average temperature for the full data set.

### C. Comparison with experiment

Figure 7(a) shows that a minimum of 1300 K is required to release helium and by 4000 K all helium is released. In contrast, the xenon data in panel (b) spans a broader range, with a minimum release temperature of only 400 K and a maximum of nearly 4500 K, at which point the ND is effectively destroyed (see Fig. 2h). The observation of two temperature clusters for xenon and a single broad distribution for helium is in good qualitative agreement with the meteoritic ND observations. To map the simulation temperatures onto their experimental equivalents, we employ the Arrhenius approach explained in the Methodology, using an activation energy of  $E_a=9$  eV. By histogram binning the simulation data in Fig. 7 and applying the transformation in Eq. 2 we

obtain a data set shown as thick blue lines in Fig. 8. On the same scale we show experimental data for the Orgueil meteorite extracted from Huss *et al.* [3, 7]. The agreement is remarkable, with the simulations reproducing all of the main meteoritic ND characteristics, including (i) the unimodal vs bimodal character, (ii) the position of the peaks, (iii) the widths of the distributions, and (iv) the maximum and minimum release temperatures. This is the first time that MD simulation has predicted these important effects.

The high level of experimental detail reproduced by the simulations provides post-hoc justification for the Arrhenius approach, confirming that the presumption of a dominant activation energy is reasonable for this class of problem. All of the predicted temperatures are correctly positioned relative to their experimental equivalents; this includes the onset of helium and xenon release, the position of the release peaks, and even the upper limit at  $\sim 1800^\circ\text{C}$ , which corresponds to destruction of the ND and the release of any remaining gases. Regarding Fig. 8(b), it is important to note that the simulations cannot predict the relative height of the peaks in the bimodal distribution, since this is function of the balance between shallow and deeply implanted xenon which is not known.

Having reproduced the essential characteristics of no-

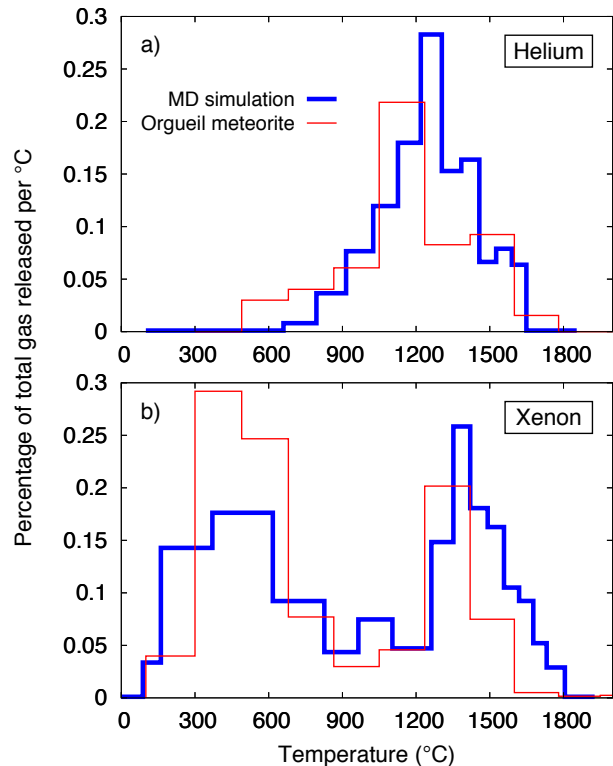


FIG. 8. Measured and simulated ND thermal release patterns for (a)  $^4\text{He}$  and (b)  $^{133}\text{Xe}$ . Experimental values (red lines) are taken from data from the Orgueil meteorite Huss *et al.* [3, 7], while the MD values (blue lines) are from this work.

ble gas release, we can address some of the most fundamental questions in the pre-solar meteoritic literature. Specifically, we can examine the atomistic origin of the Xe-P3 and Xe-HL peaks, and understand why helium exhibits unimodal behaviour. Considering first the question of xenon, the raw simulation data in Fig. 7(b) provides clues as to why release occurs at two distinct temperatures. The low-temperature peak is seen to be strongly correlated with proximity to the surface, with 4.5 Å being the critical depth beyond which low-temperature release is impossible. In contrast, high-temperature release is possible for all implantation depths, and even for depths around 1 Å there are two distinct temperature-release populations. The origin of this behaviour is that the surface of the ND progressively graphitizes with temperature, with the  $\{111\}$  face transforming prior to the  $\{100\}$  face (see Fig. 2). As a result, xenon located close to a  $\{111\}$  face can become trapped by the developing graphitic layers, and once the layer has fully formed, the xenon is too large to easily diffuse through the hexagonal graphene-like network. This effect is quantified in Fig. 9 which replots the xenon data in Fig. 7(b) for shallow depths. Panel (a) colour codes each configuration according to the closest crystallographic face, while panel (b) shows a histogram of the thermal release temperatures. It is apparent that the low-temperature peak contains roughly equal contributions from xenon near the  $\{100\}$  and  $\{111\}$  faces, while the high-temperature component is dominated by xenon close to the  $\{111\}$  face. Placing these observations in a meteoritic context, we can assert that Xe-HL is associated with either deeply buried xenon or shallow burial near a  $\{111\}$  face, while Xe-P3 sits just a few ångströms from the surface, and has no crystallographic preference.

The other major result in Fig. 7 is the prediction of

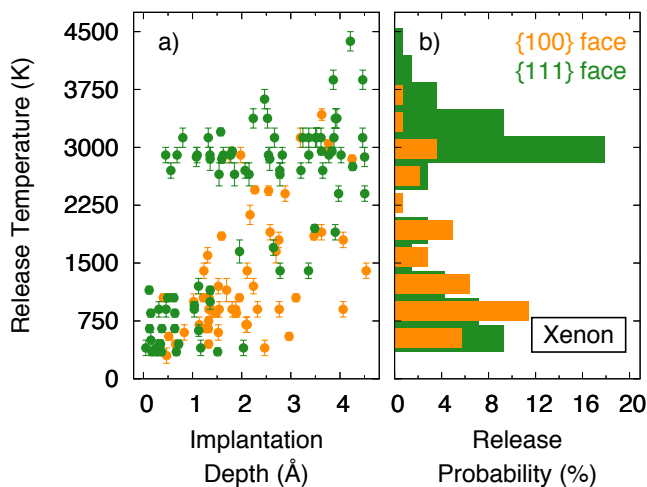


FIG. 9. (a) Classification of shallow-implantation xenon data in Fig. 7 according to proximity to a  $\{100\}$  face (orange circles) or a  $\{111\}$  face (green circles). (b) Histogram analysis of the data in (a).

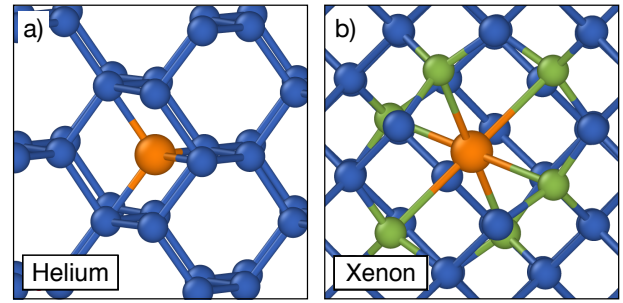


FIG. 10. (a) Tetrahedral interstitial (T-site) of helium and (b) Xe<sub>s</sub>-V defect of xenon in ND. Colour coding details are the same as Fig. 4; helium and xenon are shown as orange circles.

the unimodal release distribution for helium. Inspection of animation sequences reveals that this behaviour can be linked to the nature of the helium defect within the ND. The simulations show that helium prefers a tetrahedral interstitial (T-site) in the diamond lattice. The geometry of this defect is shown in Fig. 10(a), with the four orange lines between helium and carbon highlighting the tetrahedral symmetry. The interstitial helium diffuses amongst the  $\langle 110 \rangle$  channels in the lattice, passing through a hexagonal interstitial (H-site) transition state enroute to another T-site. This behaviour means that in the low-temperature range, the helium effectively performs a random walk around the ND. Even if the  $\{111\}$  face has graphitized, which typically occurs at around 1500 K in the simulations ( $\sim 800^\circ\text{C}$  in the experiments), the helium cannot escape through the graphitic layer. Only once the  $\{100\}$  face begins to graphitize does the helium atom escape. These observations elegantly explain why the onset of helium release is so much higher than xenon. Additionally, the smaller size of helium means that it is more mobile than xenon, which in turn explains why the peak release temperature for helium is lower than that of the corresponding xenon high-temperature peak.

The analysis of helium migration in our MD simulations is supported by density-functional-theory (DFT) calculations of noble gas defects in bulk diamond [47] which similarly conclude that helium forms an interstitial defect on the T-site and diffuses via the H-site. For xenon they find that a substitutional site is preferred and involves an adjacent vacancy, with the xenon placed at the midpoint [Fig. 10(b)]. Further DFT studies by Drumm *et al.* [48] show this configuration (Xe<sub>s</sub>-V) is substantially more stable than an alternative Xe<sub>s</sub>-3V defect involving three vacancies. Our MD approach reproduces the same behaviour as the DFT studies, including the preference for Xe<sub>s</sub>-V over Xe<sub>s</sub>-3V. Returning our attention to the simulation data in Fig. 8(b), we can assign the low-temperature xenon release peak to an Xe<sub>s</sub>-V defect near the surface. Since this defect compromises the stability of the diamond surface, the xenon is able to escape at modest temperatures of a few hundred degrees Celsius, while the helium in the T-site is far more stable.

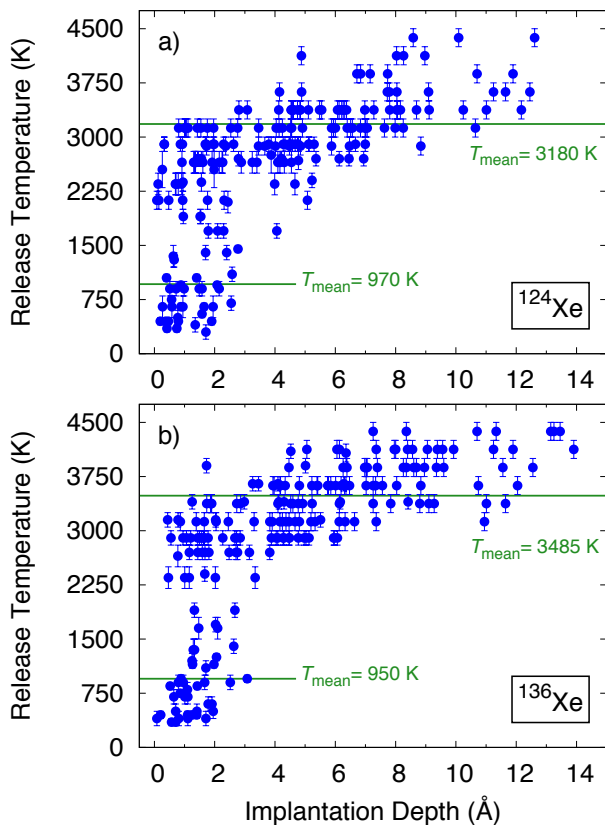


FIG. 11. Thermal release data of (a)  $^{124}\text{Xe}$  and (b)  $^{136}\text{Xe}$  as a function of implantation depth. Mean release temperatures ( $T_{\text{mean}}$ ) are shown by horizontal green lines and error bars indicate the degree of uncertainty. Due to the computational cost, the number of data points for the two isotopes is around two-thirds of that in Fig. 7(b).

The DFT study by Goss *et al.* [47] also studies other noble gases and divides them into two groups: (i) helium and neon which occupy the interstitial T-site and diffuse via the H-site, and (ii) argon, krypton and xenon which occupy substitutional sites with vacancies. This distinction between the interstitial T-site and the substitutional-vacancy provides a plausible explanation for the ND meteoritic data, where helium and neon have unimodal release peaks, while argon, krypton and xenon have bimodal distributions. To the best of our knowledge, this connection between defect type and temperature-release behaviour has not previously been made.

#### D. Isotopic effects

One of the strengths of our MD approach is the simplicity of performing virtual experiments which are challenging or even impossible in a laboratory setting. For example, obtaining isotopically pure noble gases is an expensive proposition, while with MD one can study isotopic effects easily by simply changing the mass and rerunning

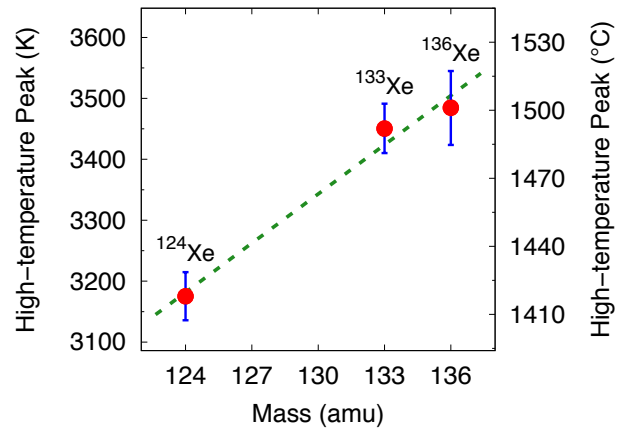


FIG. 12. High-temperature release values for three different xenon isotopes as shown in Figs. 7b and 11. Left-axis indicates raw simulation data in Kelvin while the right-axis indicates the equivalent experimental temperature in Celsius. Error bars show the standard error of the mean (SEM). The green dashed line is a linear fit to guide the eye.

the entire simulation set. To illustrate this capability, we repeated the entire implantation and thermal release protocols for  $^{124}\text{Xe}$  and  $^{136}\text{Xe}$ , both of which are naturally abundant. Thermal release data for these isotopes is shown in Fig. 11, and as seen earlier, the release profile is again bimodal. For the low-temperature peak, the release temperature is similar across all three isotopes, spanning a narrow range between 950 and 980 K, but for the high-temperature peak there is a large isotopic effect with the simulation release temperature varying from 3180 K for  $^{124}\text{Xe}$  to 3485 K for  $^{136}\text{Xe}$ . Figure 12 plots the mean release temperature for the high-temperature peak for all three xenon isotopes, with the left-axis showing the simulation temperature and the right-axis the equivalent experimental value; error bars denote the standard-error-in-the-mean. Between the lightest and heaviest isotope, the predicted temperature difference is over 80°C, sufficient to be measurable in a well-designed experiment employing isotopically pure Xe.

The isotopic effect in Fig. 12 can be plausibly attributed to the effect of mass on the vibrational frequency during thermal release. An alternative explanation focusing on implantation is less attractive, since a spectrum of implantation energies are employed and there is no obvious reason why a mass difference would generate different types of defects. Regarding the thermal release process, Fig. 4(d) (and Supplementary Movie S2) shows that the  $^{133}\text{Xe}$  atom escapes after an extended period of constant “jiggling”. For about 350 ps (between  $t = 50$  and  $t = 400$  ps), the xenon is trapped between two graphitic shells and can be seen to move back-and-forth many times before eventually escaping. This observation helps explain why the lighter Xe isotopes release at the lower temperatures as the smaller mass implies a higher vibrational frequency and hence faster reaction rate.

## IV. CONCLUSION

In this work we developed a Molecular Dynamics approach to address the important unresolved question of the origin of the unimodal and bimodal thermal release patterns of noble gases from meteoritic NDs. Our technique employs a large number (circa  $10^4$ ) of small MD simulations to calculate the thermal release pattern of implanted noble gases in ND and provides detailed atomistic insight. We reproduce the known experimental profiles for He and Xe, and propose that the nature of the noble-gas defect is the origin of the unimodal and bimodal patterns, respectively. In the case of Xe, we show that the Xe-P3 component is associated with shallow implantation on the (100) face, while the Xe-HL component is a mixture of deeply buried defects and shallow implantation on the (111) face.

The Molecular Dynamics methodology is a natural fit for cloud-computing facilities and can be easily extended to other systems where noble gases are found in pre-solar grains. In NDs, obvious directions for future work include unimodal release in  $^3\text{He}$ ,  $^{20}\text{Ne}$ ,  $^{21}\text{Ne}$  and  $^{22}\text{Ne}$  and bimodal behaviour of  $^{38}\text{Ar}$ ,  $^{36}\text{Ar}$ ,  $^{84}\text{Kr}$  and  $^{86}\text{Kr}$ . As an additional investigate tool, it is also possible to exaggerate the effect of mass, and study isotopes that do not

have a laboratory equivalent (e.g.  $^{100}\text{Xe}$ ).

Aside from NDs, there are several other important pre-solar materials where our Molecular Dynamics methodology can be applied. These include glassy carbon [49] as well as silicon carbide and graphite [1, 50–54]. All three of these pre-solar materials have high melting points and therefore are suitable for our Arrhenius-based approach. While we are unaware of any study of noble gas incorporation in these pre-solar materials, there are a number of successful atomistic simulation studies of high-temperature effects in silicon-carbide [55], graphite and carbide-derived-carbons [30, 31] and glassy carbon [26, 27, 56]. These structures provide a natural starting point for further atomistic simulations to reveal the astrophysical secrets of noble gases in pre-solar grains.

## ACKNOWLEDGEMENTS

We gratefully acknowledge many helpful discussions with Ulrich Ott and Andrey Shiryaev. NAM acknowledges fellowship FT120100924 from the Australian Research Council. Computational resources were provided by the Pawsey Supercomputing Centre with funding from the Australian Government and the Government of Western Australia.

### Supplementary Material

## Molecular dynamics approach for predicting release temperatures of noble gases in pre-solar nanodiamonds

In this Supplementary Material, we provide further information on:

- Helium–carbon and xenon–carbon interactions.
- Annealing of pristine ND
- Movies of helium and xenon release processes at high temperature.

All the equations, sections and figure in Supplementary Material are labeled with the prefix “S” to be distinguished from those that appear in the body of the paper.

### S1. HELIUM–CARBON AND XENON–CARBON INTERACTIONS

As described in the Methodology section of the main text, for the helium–carbon and xenon–carbon interactions, we use the standard Ziegler-Biersack-Littmark (ZBL) potential coupled with a Lennard-Jones (LJ) potential. The LJ potential has the form

$$U_{\text{LJ}}(r) = 4\epsilon \left\{ \left( \frac{\sigma}{r} \right)^{12} - \left( \frac{\sigma}{r} \right)^6 \right\}, \quad (\text{S1})$$

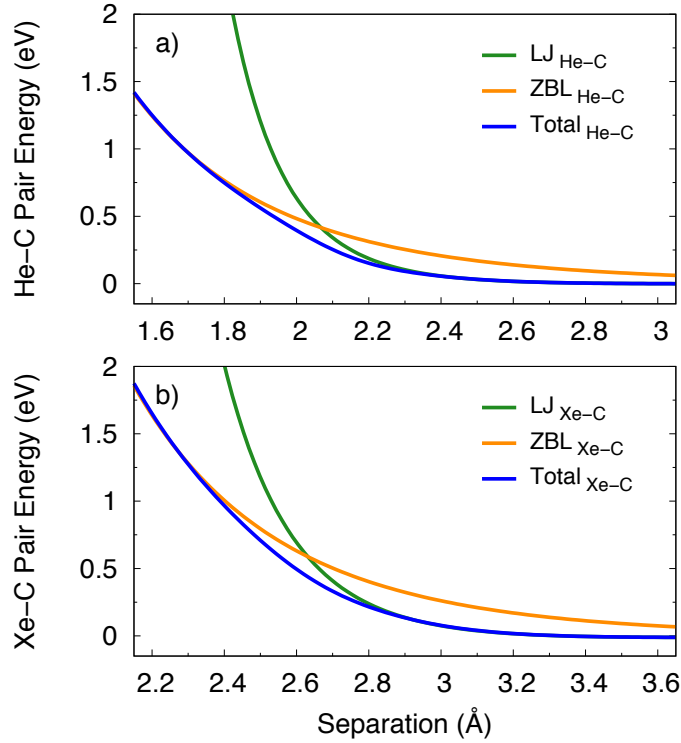


FIG. S1. Pairwise interaction energies (blue line) for (a) helium-carbon, and (b) xenon-carbon. At close approach the interaction is pure ZBL (orange line), while at distances around equilibrium and greater, a Lennard-Jones expression is used (green line).

where for helium-carbon interactions  $\varepsilon_{\text{He-C}}=0.0013$  eV and  $\sigma_{\text{He-C}}=2.98$  Å [57] and for xenon-carbon interactions  $\varepsilon_{\text{Xe-C}}=0.0114$  eV and  $\sigma_{\text{Xe-C}}=3.332$  Å [58]. Following Buchan *et al.* [22] and Christie *et al.* [32], the total interaction energy is expressed as

$$U_{\text{Total}}(r) = \left[ U_{\text{ZBL}}(r) \times f(r + \delta) \right] + \left[ U_{\text{LJ}}(r) \times (1 - f(r - \delta)) \right], \quad (\text{S2})$$

where  $f(r)$  is a Fermi-type switching function,  $\delta_{\text{He-C}}=0.09$  Å and  $\delta_{\text{Xe-C}}=0.07$  Å [33]. The Fermi function is given by

$$f(r) = \left[ 1 + \exp(b_F(r - r_F)) \right]^{-1} \quad (\text{S3})$$

where  $b_F$  controls the sharpness of the transition and  $r_F$  is the cutoff distance; these parameters are chosen manually to ensure smoothness. For Xe-C we use  $b_F=8$  Å and  $r_F=2.7$  Å, the same as our recent implantation studies [33, 36], while for He-C we use  $b_F=9.2$  Å and  $r_F=2.2$  Å. Figure S1 illustrates the He-C and Xe-C interaction energy covering the ZBL and LJ regimes. Further discussion and full details of the interpolation process are provided in Buchan *et al.* [22] and Christie *et al.* [32].

## S2. ANNEALING OF PRISTINE ND

As described in the main text, the the simulation temperatures are mapped onto their experimental equivalent using the Arrhenius relation. Calibration is performed using the graphitization of nanodiamonds (NDs) into carbon onions as a reference point. Figure 2 in the main text illustrates cross-sectional snapshots of the annealed ND for eight different temperatures. Panel (a) shows that at 1000 K there is insufficient temperature to graphitize the ND on this timescale, while at 1500 and 2000 K (panels (b) and (c)) some of the bonds on the 111 face are broken and graphitic shells form. The reason this occurs is that  $sp^3$  hybridized atoms near the surface can easily rearrange into graphite with  $sp^2$  hybridization [42, 59–61]. At higher annealing temperatures of 2500 and 3000 K (panels (d) and (e)), graphitization proceeds further inwards, creating structures with a diamond core surrounded by a graphitic shell. This core-shell structure is in good agreement with previous experimental and simulation studies [42–45, 62–65]. At

3500 K (panel (f)), a pure carbon onion (or concentric fullerene) is obtained and only a few small number of atoms ( $\sim 1\%$ ) have been lost via evaporation. At this point we have identified the temperature at which the experimental result is reproduced on the timescale that is affordable in the simulation. At the slightly higher temperature of 4000 K (panel (g)), around 8% of the atoms evaporate and the carbon atom develops a hollow core; similar structures are seen in Fig. 8(e) of Lau *et al.* [24]. At the highest temperature of 4500 K (panel (h)), the ND is completely destroyed and more than 29% of atoms are evaporated, creating a large, disordered fullerene.

### S3. SUPPLEMENTARY MOVIES

**Movie S1:** Time evolution of helium release process from  $\sim 3.9$  nm nanodiamond during the high-temperature annealing (as discussed at the Fig. 4(a) and (b) in the main text). The thickness of the slice is 1 nm. The pink lines indicate the helium trajectory, and the helium is shown as an orange circle. Carbon atoms are shown as red, green and blue circles with  $sp$ ,  $sp^2$  and  $sp^3$  hybridizations, respectively.

**Movie S2:** Time evolution of xenon release process from  $\sim 3.9$  nm nanodiamond during the high-temperature annealing (as discussed at the Fig. 4(c) and (d) in the main text). Xenon is shown as a orange circle and the pink lines indicate the xenon trajectory. The other color coding and thickness of the slice are the same as in Movie S1.

- 
- [1] Ulrich Ott. Interstellar grains in meteorites. *Nature*, 364(6432):25–33, 1993.
- [2] Roy S Lewis, Tang Ming, John F Wacker, Edward Anders, and Eric Steel. Interstellar diamonds in meteorites. *Nature*, 326:160–162, 1987.
- [3] Gary R Huss and Roy S Lewis. Noble gases in presolar diamonds I: Three distinct components and their implications for diamond origins. *Meteoritics*, 29:791–810, 1994.
- [4] Gary R. Huss and Roy S. Lewis. Presolar diamond, sic, and graphite in primitive chondrites: Abundances as a function of meteorite class and petrologic type. *Geochim. Cosmochim. Acta*, 59:115–160, 1995.
- [5] Gary R. Huss, Alex P. Meshik, Julie B. Smith, and C.M. Hohenberg. Presolar diamond, silicon carbide, and graphite in carbonaceous chondrites: implications for thermal processing in the solar nebula. *Geochim. Cosmochim. Acta*, 67(24):4823–4848, 2003.
- [6] Gary R Huss. Meteoritic Nanodiamonds: Messengers from the Stars. *Elements*, 1:97–100, 2005.
- [7] Gary R Huss and Roy S Lewis. Noble gases in presolar diamonds II: Component abundances reflect thermal processing. *Meteoritics*, 29:811–829, 1994.
- [8] D D Clayton. Origin of heavy xenon in meteoritic diamonds. *Astrophys. J.*, 540:613–619, 1989.
- [9] W. M. Howard, B. S. Meyer, and D. D. Clayton. Heavy-element abundances from a neutron burst that produces Xe-H. *Meteoritics*, 27:404–412, 1992.
- [10] Ulrich Ott. Interstellar diamond xenon and timescales of supernova eject. *Astrophys. J.*, 463:344–348, 1996.
- [11] R S Lewis and E Anders. Isotopically anomalous xenon in meteorites - A new clue to its origin. *Astrophys. J.*, 247:1122–1124, 1981.
- [12] A B Verchovsky, A V Fisenko, L F Semjonova, I P Wright, M R Lee, and C T Pillinger. C, N, and Noble Gas Isotopes in Grain Size Separates of Presolar Diamonds from Efremovka. *Science*, 281:1165–1168, 1998.
- [13] J D Gilmour, A B Verchovsky, A V Fisenko, G Holland, and G Turner. Xenon isotopes in size separated nanodiamonds from Efremovka:  $^{129}\text{Xe}^*$ , Xe-P3, and Xe-P6. *Geochim. Cosmochim. Acta*, 69:4133–4148, 2005.
- [14] A P Koscheev, M D Gromov, R K Mohapatra, and Ulrich Ott. History of trace gases in presolar diamonds inferred from ion-implantation experiments. *Nature*, 412:615–617, 2001.
- [15] A B Verchovsky, I P Wright, A V Fisenko, L F Semjonova, and C T Pillinger. Ion Implantation into Presolar Diamonds: Experimental Simulation. *Journal of Conference Abstracts*, 5:1050, 2000.
- [16] Nigel A Marks. Generalizing the environment-dependent interaction potential for carbon. *Phys. Rev. B*, 63:2879–7, 2000.
- [17] JF Ziegler, JP Biersack, and U Littmark. *The Stopping and Range of Ions in Solids.*, volume 1. Pergamon, New York, 1985.
- [18] Carla de Tomas, Irene Suarez-Martinez, and Nigel A Marks. Graphitization of amorphous carbons: A comparative study of interatomic potentials. *Carbon*, 109:681–693, 2016.
- [19] Carla de Tomas, Alireza Aghajamali, Jake L. Jones, Daniel J. Lim, Maria J. Lopez, Irene Suarez-Martinez, and Nigel A. Marks. Transferability in interatomic potentials for carbon. *Carbon*, 155:624–634, 2019.
- [20] Nigel A Marks, M Lattemann, and D R McKenzie. Nonequilibrium Route to Nanodiamond with Astrophysical Implications. *Phys. Rev. Lett.*, 108:343–5, 2012.
- [21] Barbara A Fairchild, Sergey Rubanov, Desmond W M Lau, Marc Robinson, Irene Suarez Martinez, Nigel A Marks, Andrew D Greentree, Dougal McCulloch, and Steven Praver. Mechanism for the Amorphisation of Diamond. *Adv. Mater.*, 24:2024–2029, 2012.
- [22] J T Buchan, M Robinson, H J Christie, D L Roach, D K Ross, and Nigel A Marks. Molecular dynamics simulation of radiation damage cascades in diamond. *J. Appl. Phys.*, 117:245901–9, 2015.
- [23] Blake Regan, Alireza Aghajamali, Johannes Froech, Toan Trong Tran, John Scott, James Bishop, Irene

- Suarez-Martinez, Ying Liu, Julie M. Cairney, Nigel A Marks, Milos Toth, and Igor Aharonovich. Plastic deformation of single-crystal diamond nanopillars. *Adv. Mater.*, 32:1906458, 2020.
- [24] Desmond W M Lau, Dougal McCulloch, Nigel A Marks, N R Madsen, and A V Rode. High-temperature formation of concentric fullerene-like structures within foam-like carbon: Experiment and molecular dynamics simulation. *Phys. Rev. B*, 75:035401–4, 2007.
- [25] Nigel A Marks, N C Cooper, D R McKenzie, Dougal McCulloch, P Bath, and S P Russo. Comparison of density-functional, tight-binding, and empirical methods for the simulation of amorphous carbon. *Phys. Rev. B*, 65:317–9, 2002.
- [26] T B Shiell, Dougal McCulloch, D R McKenzie, M R Field, B Haberl, R Boehler, B A Cook, C de Tomas, I Suarez Martinez, N A Marks, and J E Bradby. Graphitization of Glassy Carbon after Compression at Room Temperature. *Phys. Rev. Lett.*, 120:215701, 2018.
- [27] T B Shiell, C de Tomas, Dougal McCulloch, D R McKenzie, A Basu, I Suarez Martinez, N A Marks, R Boehler, B Haberl, and J E Bradby. In situ analysis of the structural transformation of glassy carbon under compression at room temperature. *Phys. Rev. B*, 99:024114, 2019.
- [28] Irene Suarez-Martinez and Nigel A Marks. Amorphous carbon nanorods as a precursor for carbon nanotubes. *Carbon*, 50:5441–5449, 2012.
- [29] Irene Suarez-Martinez, P J Higginbottom, and Nigel A Marks. Molecular dynamics simulations of the transformation of carbon peapods into double-walled carbon nanotubes. *Carbon*, 48:3592–3598, 2010.
- [30] Carla de Tomas, Irene Suarez Martinez, Fernando Vallejos-Burgos, María J López, Katsumi Kaneko, and Nigel A Marks. Structural prediction of graphitization and porosity in carbide-derived carbons. *Carbon*, 119:1–9, 2017.
- [31] Carla de Tomas, Irene Suarez-Martinez, and Nigel A Marks. Carbide-derived carbons for dense and tunable 3D graphene networks. *Appl. Phys. Lett.*, 112:251907–6, 2018.
- [32] H J Christie, M Robinson, D L Roach, D K Ross, Irene Suarez-Martinez, and Nigel A Marks. Simulating radiation damage cascades in graphite. *Carbon*, 81:105–114, 2015.
- [33] Jason L Fogg, Alireza Aghajamali, Jonathan A Hinks, Stephen E Donnelly, Andrey A Shiryaev, and Nigel A Marks. Modification of nanodiamonds by xenon implantation: A molecular dynamics study. *Nucl. Instrum. Methods Phys. Res. B*, 453:32–40, 2019.
- [34] Nigel A Marks and Marc Robinson. Variable timestep algorithm for molecular dynamics simulation of non-equilibrium processes. *Nucl. Instrum. Methods Phys. Res. B*, 352:3–8, 2015.
- [35] Amanda S Barnard and P Zapol. A model for the phase stability of arbitrary nanoparticles as a function of size and shape. *J. Chem. Phys.*, 121:4276–4283, 2004.
- [36] Andrey A Shiryaev, Jonathan A Hinks, Nigel A Marks, Graeme Greaves, Felipe J Valencia, Stephen E Donnelly, Rafael I González, Miguel Kiwi, Alexander L Trigub, Eduardo M Bringa, Jason L Fogg, and Igor I Vlasov. Ion implantation in nanodiamonds: size effect and energy dependence. *Sci. Rep.*, 8:992, 2018.
- [37] J.J Thomson. On the structure of the atom: An investigation of the stability and periods of oscillation of a number of corpuscles arranged at equal intervals around the circumference of a circle; with application of the results to the theory of atomic structure. *London, Edinburgh, and Dublin Philosophical Magazine and Journal of Science*, 7:237–265, 1904.
- [38] Alexander Stukowski. Visualization and analysis of atomistic simulation data with OVITO - the Open Visualization Tool. *Model. Simul. Mater. Sci. Eng.*, 18:015012, 2010.
- [39] Arthur F. Voter. Hyperdynamics: Accelerated molecular dynamics of infrequent events. *Phys. Rev. Lett.*, 78:3908–3911, 1997.
- [40] Arthur F. Voter. Parallel replica method for dynamics of infrequent events. *Phys. Rev. B*, 57:R13985–R13988, 1998.
- [41] Mads R. Sørensen and Arthur F. Voter. Temperature-accelerated dynamics for simulation of infrequent events. *J. Chem. Phys.*, 112:9599–9606, 2000.
- [42] Vladimir L. Kuznetsov, Andrey L. Chuvilin, Yuri V. Butenko, Igor Yu. Mal'kov, and Vladimir M. Titov. Onion-like carbon from ultra-disperse diamond. *Chem. Phys. Lett.*, 222:343–348, 1994.
- [43] V.L. Kuznetsov, A.L. Chuvilin, E.M. Moroz, V.N. Kolomiichuk, Sh.K. Shaikhutdinov, Yu.V. Butenko, and I.Yu. Mal'kov. Effect of explosion conditions on the structure of detonation soots: Ultradisperse diamond and onion carbon. *Carbon*, 32:873–882, 1994.
- [44] Satoshi Tomita, Andrzej Burian, John C Dore, David LeBolloch, Minoru Fujii, and Shinji Hayashi. Diamond nanoparticles to carbon onions transformation: X-ray diffraction studies. *Carbon*, 40:1469–1474, 2002.
- [45] Zhijun Qiao, Jiajun Li, Naiqin Zhao, Chunsheng Shi, and Philip Nash. Graphitization and microstructure transformation of nanodiamond to onion-like carbon. *Scr. Mater.*, 54:225–229, 2006.
- [46] J Xiao, G Ouyang, P Liu, C X Wang, and G W Yang. Reversible Nanodiamond-Carbon Onion Phase Transformations. *Nano Lett.*, 14:3645–3652, 2014.
- [47] J. P. Goss, R. J. Eyre, P. R. Briddon, and Alison Mainwood. Density functional simulations of noble-gas impurities in diamond. *Phys. Rev. B*, 80:085204, 2009.
- [48] D W Drumm, M C Per, S P Russo, and L C L Hollenberg. Thermodynamic stability of neutral Xe defects in diamond. *Phys. Rev. B*, 82:054102–6, 2010.
- [49] Rhonda M Stroud, Matthew F Chisholm, Philipp R Heck, Conel M O'D Alexander, and Larry R Nittler. Supernova shock-wave-induced CO-formation of glassy carbon and nanodiamond. *Astrophys. J*, 738:L27, 2011.
- [50] Ulrich Ott. Presolar Grains in Meteorites and Their Compositions. *Space Sci. Rev.*, 130:87–95, 2007.
- [51] Ulrich Ott. Planetary and pre-solar noble gases in meteorites. *Chem Erde-Geochem.*, 74:519–544, 2014.
- [52] Andrew M. Davis. Stardust in meteorites. *Proc. Natl. Acad. Sci.*, 108:19142–19146, 2011.
- [53] Sachiko Amari, Edward Anders, Alois Virag, and Ernst Zinner. Interstellar graphite in meteorites. *Nature*, 345:238–240, 1990.
- [54] Sachiko Amari, Peter Hoppe, Ernst Zinner, and Roy S Lewis. The isotopic compositions and stellar sources of meteoritic graphite grains. *Nature*, 365:806–809, 1993.
- [55] Kazunori Fujisawa, Yu Lei, Carla de Tomas, Irene Suarez Martinez, Chanjing Zhou, Yu-Chuan Lin, Shruti Subramanian, Ana Laura Elías, Masatsugu Fujishige, Kenji Takeuchi, Joshua A Robinson, Nigel Anthony

- Marks, Morinobu Endo, and Mauricio Terrones. Facile 1D graphene fiber synthesis from an agricultural by-product: A silicon-mediated graphenization route. *Carbon*, 142:78–88, 2019.
- [56] X Huang, T B Shiell, C de Tomas, I Suarez-Martinez, S Wong, S Mann, D R McKenzie, N A Marks, D G McCulloch, and J E Bradby. The mechanical response of glassy carbon recovered from high pressure. *J. Appl. Phys.*, 127:145105, 2020.
- [57] Thanh X Nguyen, Nathalie Cohaut, Jun-Seok Bae, and Suresh K Bhatia. New Method for Atomistic Modeling of the Microstructure of Activated Carbons Using Hybrid Reverse Monte Carlo Simulation. *Langmuir*, 24:7912–7922, 2008.
- [58] Vahan V Simonyan, J Karl Johnson, Anya Kuznetsova, and John T Yates Jr. Molecular simulation of xenon adsorption on single-walled carbon nanotubes. *J. Chem. Phys.*, 114:4180–4185, 2001.
- [59] C Z Wang, K M Ho, M D Shirk, and P A Molian. Laser-Induced Graphitization on a Diamond (111) Surface. *Phys. Rev. Lett.*, 85:4092–4095, 2000.
- [60] C Pantea, J Qian, G A Voronin, and T W Zerda. High pressure study of graphitization of diamond crystals. *J. Appl. Phys.*, 91:1957–1962, 2002.
- [61] Amanda S Barnard, S P Russo, and I K Snook. Structural relaxation and relative stability of nanodiamond morphologies. *Diam. Relat. Mater.*, 12:1867–1872, 2003.
- [62] Jan H. Los, Luca M. Ghiringhelli, Evert Jan Meijer, and A. Fasolino. Improved long-range reactive bond-order potential for carbon. i. construction. *Phys. Rev. B*, 72:214102, 2005.
- [63] A Bródka, T W Zerda, and A Burian. Graphitization of small diamond cluster — Molecular dynamics simulation. *Diam. Relat. Mater*, 15:1818–1821, 2006.
- [64] A Bródka, L Hawelek, A Burian, S Tomita, and V Honkimäki. Molecular dynamics study of structure and graphitization process of nanodiamonds. *J. Mol. Struct.*, 887:34–40, 2008.
- [65] P Ganesh, P R C Kent, and Vadym N Mochalin. Formation, characterization, and dynamics of onion-like carbon structures for electrical energy storage from nanodiamonds using reactive force fields. *J. Appl. Phys.*, 110:073506–9, 2011.